Structural changes of poly(butadiene)-poly(ethyleneoxide) diblock-copolymer micelles induced by a cationic surfactant: Scattering and cryogenic transmission electron microscopy studies

Anette Nordskog, Holger Egger, Gerhard H. Findenegg, and Thomas Hellweg*
TU Berlin, Stranski-Laboratorium f. Physikalische und Theoretische Chemie, Strasse des 17.Juni 112, D-10623 Berlin, Germany

Helmut Schlaad
Max-Planck-Institut für Kolloid- und Grenzflächenforschung, Abteilung Kolloidchemie, Am Mühlenberg 1, D-14476 Golm, Germany

Hans von Berlepsch and Christoph Böttcher
Freie Universität Berlin, Forschungszentrum für Elektronenmikroskopie, Fabeckstrasse 36a, D-14195 Berlin, Germany
(Received 1 March 2002; revised manuscript received 19 March 2003; published 24 July 2003)

Micelles of the diblock copolymer poly(butadiene)-poly(ethyleneoxide) (B_{40}-*b*-EO_{62}) and mixed micelles of this polymer with the cationic surfactant dodecyltrimethylammonium bromide (C_{12}TAB) were investigated using static and dynamic light scattering and small-angle neutron scattering. It is shown that the surfactant induces a major structural change from large mainly rodlike aggregates to smaller spherical mixed micelles. The rodlike assemblies found in the absence of surfactant have a contour length L of ca. 500 nm and a diameter $d \approx 30$ nm. The spherical mixed micelles obtained upon addition of C_{12}TAB possess a hydrodynamic radius of 15 nm and still contain several polymer molecules. The results of the scattering experiments are consistent with observations of the aggregates by cryogenic transmission electron microscopy.

DOI: 10.1103/PhysRevE.68.011406 PACS number(s): 82.70.−y, 81.07.−b, 61.12.Ex, 66.10.−x

I. INTRODUCTION

Self-assembly phenomena in colloidal [1–5] and polymer-based systems [6–8] have attracted much attention in recent years. A multitude of different microstructures was found in solutions of block copolymers [6,9–11] and there is growing interest in using them as templates for the preparation of mesoscopically structured organic or inorganic hybrid materials [12–18]. To our knowledge, most studies of nanocasting start from spherical particles, but recently materials based on ordered three-dimensional arrangements of cylinders were also prepared [8]. However, not much is known about the control of the structuring process, especially in the case of polymer-based systems and cylindrical shapes. The most important parameters for the control of micellar shape in diblock-copolymer solutions appear to be the cross-sectional area of the hydrophilic chain (''head group'') and the ratio of the lengths of the two building blocks. This is similar to the situation in solutions of low-molecular-weight surfactants. For several nonionic surfactants (e.g., the group of alkyl oligo ethyleneoxide C_iE_j), the area per head group is changed with temperature (due to a change in hydration) and thus the micelles transform from spherical to wormlike shape as the temperature is increased in the isotropic solution phase of the phase diagram [19–21] as the temperature is increased. In the case of diblock copolymers containing a charged block, the structure of the micellar aggregates can be controlled by the addition of salt and transitions from spherical micelles to rodlike and wormlike structures have been observed at high salt concentrations [22].

In the present paper, a different approach to the control of the self-assembly process found in diblock-copolymer (BCP) solutions is presented. By addition of low-molecular-weight amphiphiles to such a polymer solution, it is possible to alter the packing parameter in the micellar structures. This so-called concept of comicellization was already used before using the anionic surfactant sodium dodicyl-sulfate (SDS) (see Refs. [23–26] and references therein) and especially interesting is its application in the preparation of microemulsions [27,28]. In microemulsions, addition of copolymers can largely reduce the necessary amount of surfactant to solubilize the added oil.

In the present study, we focus on the change in shape upon addition of the cationic low-molecular-weight surfactant dodecyltrimethylammonium bromide (C_{12}TAB) to rodlike, large poly(butadiene)-poly(ethyleneoxide) (B_{40}-*b*-EO_{62}) micelles. Preliminary results obtained with a PB-PEO diblock copolymer of slightly different block length have been reported in a recent paper [29]. Here, we present a more quantitative analysis of the observed structures using a combination of elastic and inelastic scattering techniques. Moreover, the observed scattering behavior will be used to characterize the structures with regard to their shape by applying rather simple hydrodynamic model calculations [30–34]. Additionally, the occurring structures are directly visualized by cryogenic transmission electron microscopy (cryo-TEM).

II. THEORY

A. Small-angle neutron scattering (SANS)

Small-angle scattering curves obtained from solutions of particles exhibiting a low polydispersity can be represented by

$$I(q) = A(\bar{\rho} - \rho_0)^2 V^2 N S(q) P(q), \tag{1}$$

*Author to whom correspondence should be addressed. Electronic address: thomas.hellweg@tu-berlin.de

where the interparticle structure factor $S(q)$ and the particle form factor $P(q)$ are functions of the scattering vector q given by

$$q = \frac{4\pi}{\lambda}\sin\left(\frac{\theta}{2}\right), \tag{2}$$

with θ the scattering angle and λ the neutron wavelength. $\overline{\rho}$ is the scattering length density of the particles, ρ_0 that of the solvent. N is the particle number and V their respective volume. The constant A contains experimental factors. For low concentration and intermediate or large values of q, the interparticle structure factor $S(q) \approx 1$ and therefore the analysis of the experiments has mainly to deal with the particle form factor [35,36].

Some information about the shape of the diblock-copolymer aggregates is revealed by the determination of the scattering exponent α in the low-q regions of the experimental data, where

$$I(q) \propto \frac{1}{q^{\alpha}}. \tag{3}$$

One expects α to be 0 for spheres, 1 for rodlike shapes, and 2 for flat structures [37]. In addition, a Guinier analysis can be performed in the intermediate q region of the spectra ($qR \approx 1$) using the equation

$$I(q) \propto \exp(-q^2\Lambda). \tag{4}$$

In this relation, Λ is a length scale parameter, which can be connected with the respective scattering aggregate by $\Lambda = R_g^2/3$ for spheres and by $\Lambda = R_{cs}^2/2$ for rodlike objects, where R_g is the radius of gyration of the sphere and R_{cs} is the cross-sectional radius of the rod [37,38]. A complete description of the scattering curves can be achieved by fitting or simulating the entire experimental data using analytical expressions for the form factor $P(q)$. In the present study for spherical aggregates exhibiting a low polydispersity, an analytical solution of the integral

$$P_{\sigma,R_0}(q) = \frac{9}{\sqrt{(2\pi\sigma^2)}}\int_0^{\infty}\left[\frac{\sin(qR) - qR\cos(qR)}{(qR)^3}\right]^2 \times \exp\left(-\frac{(R-R_0)^2}{2\sigma^2}\right)dR \tag{5}$$

was used for the fitting procedure. The polydispersity is modeled by a Gaussian distribution [39]. For a sample containing two different well-defined populations of spherical particles at low concentrations, the scattering curves can be described by a simple sum of two of these form factor contributions [again neglecting influences from $S(q)$].

A third more general way to obtain information from the small-angle scattering curves, which was used in this work, is the generalized indirect Fourier transformation method developed by Glatter [40–43]. This numerical approach directly yields the pair distribution function $p(r)$ of the scattering particles.

B. Light scattering

1. Static light scattering (SLS)

The static scattering from a liquid arises from inhomogeneities due to fluctuations of the density or the concentration c [44]. For rather small particles, an analysis of the angle dependence of the scattered intensity can yield the radius of gyration R_g of the particles. Commonly, the static light scattering data can be analyzed based on the relation

$$\frac{Kc}{R_\theta} = \frac{1}{M} + 2Bc, \tag{6}$$

where R_θ is the Rayleigh ratio [45] and K contains all optical properties of relevance for the experiment. The above is valid for particles with $R_g \ll \lambda$. For larger particles a form factor has to be taken into account,

$$\frac{Kc}{R_\theta} = \frac{1}{P(\theta)}\left[\frac{1}{M} + 2Bc\right]. \tag{7}$$

Using the Debye approximation for the form factor $P(\theta)$ is the basis for the so-called Zimm plot, which can be applied to extract R_g and the apparent molar mass from the static light scattering data [44]. The molar mass yields the aggregation number of the aggregates.

For large particles, the approach described in Sec. II A can be applied using Eq. (7) to obtain $P(\theta)$ by extrapolation to zero concentration. In this work, the SLS form factor curves of the pure diblock-copolymer solutions are fitted using the Koyama form factor for stiff chain molecules or structures [46].

2. Photon correlation spectroscopy

The normalized electrical field autocorrelation function $g^1(\tau)$ contains the information about the dynamics of the scattering system. $g^1(\tau)$ can be computed from the respective intensity time correlation function $g^2(\tau)$ by the Siegert relation. In the case of a monodisperse ideal sample, $g^1(\tau)$ is represented by a single exponential:

$$g^1(\tau) = \exp(-\Gamma\tau) \tag{8}$$

with $\Gamma = D^T q^2$, D^T the translational diffusion coefficient, and q the scattering vector [47–49]. Normally, samples are polydisperse and the decay of the correlation function must be described by a weighted sum of exponentials,

$$g^1(\tau) = \int_0^{+\infty} G(\Gamma)\exp(-\Gamma\tau)d\Gamma, \tag{9}$$

where $G(\Gamma)$ is the distribution function of the relaxation rates.

An analysis of this distribution of relaxation rates can be performed using the method of cumulants [50], the analysis

by an inverse Laplace transformation of Eq. (9) by the use of the FORTRAN program CONTIN [51,52], or by the ORT procedure suggested by Glatter [40,41]. From the mean value $\overline{\Gamma}$ one obtains the translational diffusion coefficient D^T,

$$\overline{\Gamma} = D^T q^2, \tag{10}$$

and the hydrodynamic radius R_h making use of the Stokes-Einstein equation,

$$D^T = \frac{kT}{6\pi\eta R_h}, \tag{11}$$

with η being the viscosity and k the Boltzmann constant. The equivalent equation for the rotational diffusion coefficient D^R has the form

$$D^R = \frac{kT}{8\pi\eta R_h^3}. \tag{12}$$

The dependence on R_h^3 makes D^R more sensitive to structural changes compared to D^T.

For weakly interacting particles and low concentrations, the concentration dependence of D^T can be described by

$$D^T_{exp} = D^T_0(1 + k_D[C]), \tag{13}$$

where the diffusional virial coefficient k_D includes thermodynamic and frictional effects on D_{exp}. For stronger interactions, this linearization may not hold.

C. Hydrodynamic models

Several models are available for the calculation of the transport properties of anisometric structures. The earliest of these was the Perrin description of symmetrical ellipsoids [32–34]. For prolate (cigarlike) particles, the transport coefficients for rotational and translational motions are connected with molecular dimensions by

$$D^T = \frac{kT}{6\pi\eta R_h}\Phi(\rho), \tag{14}$$

$$D^R = \frac{kT}{8\pi\eta R_h^3}\left[\frac{2}{3}\left(\frac{(2-\rho^2)\Phi(\rho)-1}{(1-\rho^4)}\right)\right], \tag{15}$$

where $\rho \equiv b/a$ is the axial ratio of the ellipsoid. a denotes the length of the major axis of the particle and b is the length of the two minor axes.

Hence, these relations are corrections of the Stokes-Einstein equations for translational and rotational diffusion using a frictional form factor given by

$$\Phi(\rho) = (\rho^2-1)^{-1/2}\arctan[(\rho^2-1)^{1/2}]. \tag{16}$$

For cylinders, several different descriptions are available starting with the approach by Riseman and Kirkwood [53] based on the modeling of the rod by a linear assembly of spherical beads leading to

$$D^T = \frac{kT}{3\pi\eta L}\ln\left(\frac{L}{d}\right) \tag{17}$$

and

$$D^R = \frac{3kT}{\pi\eta L^3}\ln\left(\frac{L}{d}\right). \tag{18}$$

Here, L and d represent the length and the thickness of the cylinder. According to this model,

$$D^R = \frac{9D^T}{L^2}. \tag{19}$$

A second model for cylinders with $L/d \geqslant 9$ was derived by Broersma [30,31]. However, this model does not provide a significantly better representation of the data than the Kirkwood-Riseman approach, even in its corrected form [54]. A further approach for the description of transport properties of cylinders in solution is the model presented by Tirado and Garcia de la Torre, which is valid for the region $2 \leqslant L/d \leqslant 20$ [55–57]. In this model, the translational diffusion coefficient is connected to the particle dimensions by

$$D^T = \frac{kT}{3\pi\eta L}\left[\ln\left(\frac{L}{d}\right) + \nu^T\right],$$

$$\nu^T = 0.312 + \frac{0.565}{\frac{L}{d}} - \frac{0.100}{\left(\frac{L}{d}\right)^2}. \tag{20}$$

A similar equation was derived for the rotational diffusion,

$$D^R = \frac{3kT}{\pi\eta L^3}\left[\ln\left(\frac{L}{d}\right) + \nu^R\right],$$

$$\nu^R = -0.662 + \frac{0.917}{\frac{L}{d}} - \frac{0.050}{\left(\frac{L}{d}\right)^2}. \tag{21}$$

The transport coefficients D^T and D^R can be connected by defining the function

$$\zeta\left(\frac{L}{d}\right) = \left(\frac{9\pi\eta}{kT}\right)^{2/3}\frac{D^T}{(D^R)^{1/3}}. \tag{22}$$

All the above models allow for a determination of the molecular dimensions, when both diffusion coefficients are known or may be used to determine the length or thickness of the formed aggregates as by adjusting the values to reproduce one of the measured diffusion coefficients. This is useful in cases when the rotational diffusion coefficient is not available.

III. MATERIALS AND METHODS

A. Sample preparation

1. Synthesis and characterization of B_{40}-*b*-EO_{62}

The poly(butadiene)-*b*-poly(ethyleneoxide) block copolymer B_{40}-*b*-EO_{62} was prepared by sequential anionic polymerization of 1,3-butadiene ($-78\,^{\circ}C$) and ethyleneoxide ($+40\,^{\circ}C$) in tetrahydrofuran with *sec*-butyllithium/*t*-BuP_4 phosphazene as the initiator [58]. For purification, the aqueous solution of the crude material was thoroughly washed with the strongly acidic cation exchanger DOWEX 50WX4-100 (Sigma) to extract protonated *t*-BuP_4 traces, ultrafiltrated with bidistilled water (molecular weight cutoff: 10^3 Da), and freeze dried [59].

The microstructure of the PB segment is 90% *trans*-1,2 and 10% *trans*-1,4 as revealed by ^{1}H nuclear magnetic resonance (NMR) (400.1 MHz, 25 °C, $CDCl_3$). The average number of B units (40) was determined by size exclusion chromatography (SEC) [eluent, $CHCl_3$ at a flow rate of 1 ml/min; columns, 30×0.8 cm^2; 5-μm MZ-SDplus, 10^3, 10^5, 10^6 Å; detectors, UV and RI; calibration, poly(1,2-butadiene)] on the PB precursor sample, which was taken from the polymerization reactor prior to EO addition. From the number of B units and the mole fraction of EO in the copolymer (0.608, ^{1}H NMR), the average number of EO units was calculated to be 62. The apparent polydispersity index (ratio of weight- to number-average molecular weights, M_w/M_n, of the copolymer is 1.07 (SEC).

2. Other materials

The cationic surfactant C_{12}TAB was purchased from Aldrich Chemicals and used without further purification (purity $\geqslant 97\%$).

High purity water from a Milli-*Q* water purification system by Millipore/Waters was used as the solvent for all light scattering experiments. For neutron scattering experiments, the samples were dissolved in D_2O from Sigma Fine Chemicals (isotopic purity $\geqslant 99.8\%$).

3. Samples for light scattering experiments

Samples were prepared by dilution of the original aqueous solution of 2 wt % of the block copolymer to a stock solution of 0.2 wt %, which was further diluted to obtain samples with the polymer concentrations 0.2, 0.16, 0.12, 0.08, 0.04, and 0.02 wt %. Surfactant was added to the solutions in two different ways, hereafter denoted as methods *A* and *B*.

Method A. Pure surfactant was added to a small volume of the original polymer solution to obtain a surfactant concentration above the critical micellar concentration (CMC). This solution was diluted by water to the stock solution of polymer concentration 0.2 wt % and a surfactant concentration below the CMC. The resulting stock solution of the mixed system (block copolymer plus surfactant) was then further diluted to investigate the concentration dependence of the aggregate structures by light scattering.

Method B. The surfactant was added to the 0.2% stock solution of the polymer in such a way that the surfactant concentration in the samples never exceeded the CMC. The respective samples prepared by methods *A* or *B* had the same concentrations of polymer and surfactant, and differed only in the way of preparation.

All samples for the light scattering experiments except the pure polymer solutions were directly filtered into dust-free cylindrical quartz cells with an inner diameter of 0.8 cm using filters with a pore size of 200 nm (Schleicher & Schuell, Spartan 30/0.2 RRC). The pure polymer solutions were not filtered because of their high viscosity and in order to avoid a change of the concentration by filtration.

In this work, the concentrations of block copolymer and surfactant are expressed by the polymer mass concentration and the ratio of the mass concentration of surfactant and block copolymer, given as the ratio r_m defined by

$$r_m=\frac{[C_{C_{12}TAB}]}{[C_{polymer}]}. \tag{23}$$

4. Samples for SANS

For the neutron scattering experiments, only the 2 wt % samples prepared according to method *A* without dilution were used. In SANS experiments diluted samples would exhibit a very low scattering intensity, which leads to unacceptably high measuring times. Therefore, in contrast to the samples for light scattering experiments, these samples were not diluted. That is why in these samples, the concentration of the low-molecular-weight surfactant is above the CMC.

Scattering contrast for the small-angle neutron scattering experiments was generated by making use of D_2O as the solvent.

B. Cryo-TEM

The samples for cryo-TEM were prepared at room temperature by placing a droplet (10 μl) of the polymer solution on hydrophilized perforated carbon film grids (60-s plasma treatment at 8 W using a BALTEC MED 020 device). The excess fluid was blotted off to create an ultrathin layer (typical thickness of 100 nm) of the solution spanning the holes of the carbon film. The grids were immediately vitrified in liquid ethane at its freezing point ($-184\,^{\circ}C$) using a standard plunging device. Ultrafast cooling is necessary for an artifact-free thermal fixation (vitrification) of the aqueous solution avoiding crystallization of the solvent or rearrangement of the assemblies. The vitrified samples were transferred under liquid nitrogen into a Philips CM12 transmission electron microscope using the Gatan cryoholder and stage (model 626). Microscopy was carried out at $-175\,^{\circ}C$ sample temperature using the microscopes' low dose protocol at primary magnifications of 58 300*x* (see Fig. 1) or 33 000*x* (see Fig. 2). The defocus was chosen to be 1.2 μm corresponding to a first zero of the phase contrast transfer function at 2.1 nm.

C. Light scattering

1. Photon correlation spectroscopy

Light scattering measurements were performed using commercial equipment for simultaneous static and dynamic

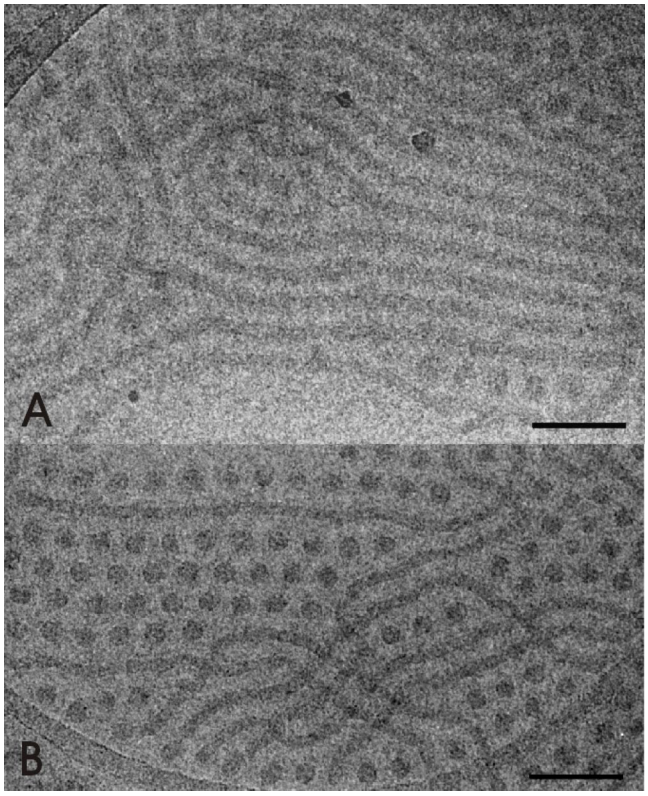

FIG. 1. Cryo-TEM micrographs of a 0.1 wt % pure polymer solution. The letters *A* and *B* indicate two different preparations. Two micellar species can be identified: long wormlike or rodlike particles and smaller spherical structures. The diameter of the rodlike particles is ≈33.4 nm. The diameter of the spherical particles is ≈38.2 nm. The spherical micelles exhibit a rather low polydispersity. (The black bar represents 100 nm.)

light scattering experiments from ALV-Laservertriebsgesellschaft (Langen, Germany). The light source employed was the green line ($\lambda = 532$ nm) of a Coherent Compass 315M-150 frequency doubled diode pumped solid state laser, operating with a constant output power of 150 mW. Temperature control of the samples better than 0.1 K was achieved using a toluene bath connected to a Lauda RCS6 thermostat. The toluene also served as an index matching bath. The scattered light was detected with a photomultiplier tube (Thorn EMI) mounted on a goniometer arm, operated in single-photon-counting mode. The preamplified fluctuating intensity signal was then time autocorrelated using an ALV-5000 multiple τ hardwire correlator (256 channels, first lag time 200 ns). Dynamic light scattering (DLS) experiments were performed in an angular range of $30° < \theta < 150°$.

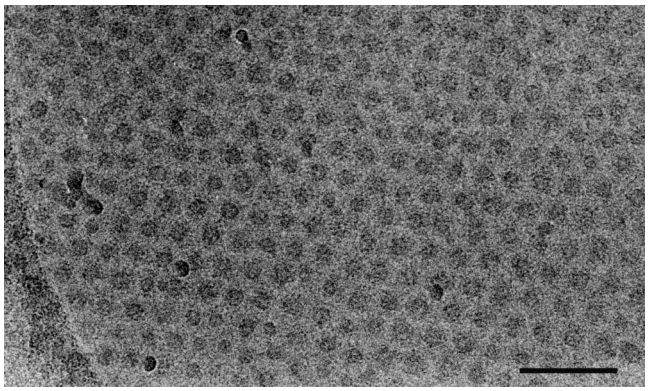

FIG. 2. Cryo-TEM micrograph of a solution containing both, polymer and C_{12}TAB (C_{12}TAB concentration below the CMC). Only spherical micelles are observable. The total diameter of the micelles is ca. 33.5 nm. (The black bar represents 100 nm.)

2. Static light scattering

For the static light scattering (LS) experiments, the static (integrated) intensity was normalized to the primary beam intensity and brought to an absolute scale by using a toluene reference for calibration [45]. Consequently, the primary beam intensity had to be monitored, which was done by means of a beam splitter and a four-segment photodiode. Static LS measurements were carried out in an angular range of $20° < \theta < 150°$, corresponding to a scattering vector range of $0.008 < q < 0.03$ nm^{-1}. The refractive index increment dn/dc, which is needed for the calculation of the contrast factor K, was measured with a commercial refractometer (Baur Electronics).

D. Small-angle neutron scattering

Small-angle neutron scattering experiments were carried out at the "Laboratoire Léon Brillouin–Laboratoire Commun CEA-CNRS" (LLB) using the PAXY machine. This small-angle scattering machine is installed on the neutron guide G2 (cold source) of the Orphée reactor and was designed for high resolution in q space. Making use of a mechanical selector, the neutron wavelengths were chosen to be 6 Å, 10 Å, and 12 Å. The wavelength spread was ≈±10%. All measurements were made at three sample to detector distances (1.05 m, 3.20 m, and 6.70 m) changing the wavelength and the sample to detector distance simultaneously and therefore covering a q range from 0.004 Å^{-1} to 0.347 Å^{-1}. The data were collected on a two-dimensional multiwire detector containing BF_3. For more details of the experimental setup, see the relevant publications of the LLB (e.g., Ref. [60]).

The raw data were corrected for the efficiency of the different detector cells using a water spectrum and then, because of the isotropic character of the scattering from the diblock-copolymer solutions or copolymer-surfactant mixtures, they were circularly averaged. After correction for the scattering of the solvent and the empty cell, the data were brought to an absolute scale. Calibration of the data was done according to the procedure described by Cotton [61]. This calibration is based on the determination of an attenuation factor of the primary beam intensity. All the data reduction steps described above were done using software provided by the LLB.

IV. RESULTS AND DISCUSSION

A. Cryo-TEM

1. Pure polymer solutions

Two cryo-TEM images of a 0.1 wt % pure polymer solution are presented in Figs. 1(a,b). Both images show long

wormlike or rodlike micelles that coexist with spherical micelles, but the numbers of the two species are markedly different in the two images. A qualitatively similar morphology has been found for 0.02 and 0.2 wt % polymer solutions. In particular, the coexistence of spherical and wormlike micelles exhibiting comparable geometry and size has been confirmed. The wormlike micelles tend to be disposed parallel to each other and the spherical micelles fill the remaining space, either arranged in strings of pearls or in regular hexagonal arrays. Similar ordering effects were observed by Zheng *et al.* [62] in other BCP systems and were explained by the miniscuslike thickness gradient of the sample layer, induced in the blotting process, in which the aggregates are forced away from the thin central region towards the thicker edges. As a consequence, all aggregates are brought into close packing. An intriguing finding of this arrangement of aggregates is that the next-neighbor distance is nearly constant. This observation may be explained by postulating an outer shell of low contrast surrounding the high-contrast core of the aggregates and that the ordered packing of the aggregates results from a close packing of shells. An estimate of the size of the two blocks of the polymer shows that the high-contrast part of the aggregates can be attributed to the PB domains, i.e., the core of the micelles, but is too small to accommodate the complete polymer. We therefore conclude that the bright regions surrounding the cores, which are of obviously similar density as the embedding solvent and are therefore not discernible from the background, should be attributed to the PEO domain. Taking the distance between the centers of neighboring micelles as the total cross-sectional diameter, and the width of the dark part as the core diameter of the aggregates, we obtain a total diameter of 33.5 nm for the rodlike aggregates and 38.0 nm for the spherical micelles. The respective mean core diameters are 12.0 nm and 21.0 nm. The uncertainty of these values is estimated to be less than 10%. Because of the ordering effect in the cryo-TEM preparation mentioned above, quantitative estimates of the number ratio of coexisting wormlike and spherical species are far too speculative [63]. However, since the scattering intensity from a given particle depends on the sixth power of the particle size, it will be assumed in the analysis of the static light and neutron scattering data that the contribution to the scattering intensity from spherical micelles can be neglected in good approximation.

The observed elongated structures [see Figs. 1(a,b)] correspond to those found in the solutions of B_{45}-*b*-EO_{56} by Zheng and co-workers [62] also using cryo-TEM and to the structures identified in Ref. [29] using atomic force microscopy (AFM). The AFM measurements were done with the solutions of B_{37}-*b*-EO_{53}. In contrast to the present work in the studies mentioned above, no spherical aggregates but only rodlike structures were observed.

A possible explanation for this phenomenon is that the polymer investigated here has a slightly larger head group compared to the other two systems. In the present study, the ratio N_B/N_{EO} of the degrees of polymerization of the two blocks is 0.645. In the other two studies, the ratios were 0.7 [29] and 0.8 [62]. This may already allow for the formation of spherical structures with a higher overall curvature and thus lead to a coexistence of rodlike and spherical aggregates.

These observations are in qualitative agreement with the results from DLS experiments presented and discussed in Sec. IV D 1.

2. Polymer-Surfactant mixtures

A representative cryo-TEM micrograph of a mixed solution of polymer (0.2 wt %) and surfactant ($r_m = 25$) is shown in Fig. 2. The first striking observation is the complete disappearance of elongated structures upon addition of C_{12}TAB. Only a regularly hexagonally packed array of spherical objects can be observed. The total diameter of the spheres was calculated to be 33.5 nm and the core diameter was estimated to be 17.0 nm. The uncertainty of these values is again $\approx \pm 10\%$. Thus the dimensions of the micelles are about 13% and 20% smaller than the respective values of the spherical micelles in the pure polymer solution.

B. Static light scattering

As the micellar aggregates of the pure polymer investigated in the present study are in general too large to fulfill the relation $R_g \ll \lambda$, the Zimm formalism was only used to extrapolate to zero concentration in case of the pure polymer solutions. This is of course a rather rough, but nevertheless, justified approximation because the size and shape of the aggregates seems to remain unaffected by dilution over a wide concentration range (see also results from dynamic light scattering).

For the mixed micelles, the Zimm plot was used to determine R_g, since the mixed micelles are somewhat smaller than those of the pure polymer. However, the values obtained in this way can only be taken as qualitative measures. The reason for this becomes obvious looking at Fig. 3. For the mixed micelles, the linearization which is used to obtain a value for R_g does not lead to a good representation of the data.

1. Pure polymer solutions

The analysis of the static light scattering data from the pure polymer solutions is based on the assumption that the scattering intensity from these samples is largely dominated by the scattering from the rodlike aggregates. This assumption is justified, since the scattering intensity from a specific particle depends roughly on the sixth power of its radius. From the cryo-TEM images [see Figs. 1(a) and 1(b)], it can be easily estimated that the radius of gyration of the elongated structures will be at least two times higher than that of the spherical aggregates. Hence, for equal particle numbers of spherical and elongated structures, the rodlike particles will exhibit a scattering intensity which is ≈ 64 times greater than the intensity scattered from the spherical particles. It, therefore, appears to be justified to neglect the spherical particles in the analysis of the light scattering data, even though the relative numbers of spherical and cylindrical particles are not known.

A solution of pure polymer (B_{40}-*b*-EO_{62}) in water was analyzed using a Zimm plot, in which the measured values

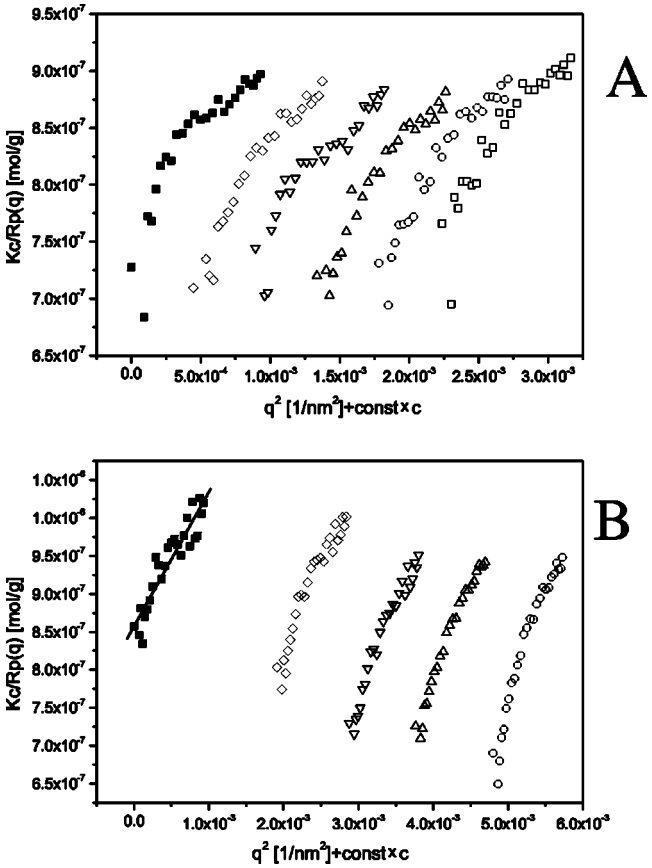

FIG. 3. Zimm plots of the static light scattering data for polymer-surfactant mixtures of constant surfactant-to-polymer ratio (*A*, $r_m=6$; *B*, $r_m=32$).

are plotted as a function of concentration and of scattering vector q. For sufficiently small particles ($R_g<\lambda/20$), such a plot can then be utilized to extrapolate to zero concentration and $\theta=0°$, which leads to a value for the molar mass of the sample from the intercept of both extrapolated curves. From the slope of the extrapolated curve obtained for $c=0$, one usually obtains the radius of gyration for the sample. However, as already mentioned in the introduction of this section, the aggregates are too large and therefore the extrapolated curve is not linear.

In Fig. 4, the extrapolated curve for $c=0$ from the Zimm plot for the B_{40}-*b*-EO_{62} solutions (data not shown) is plotted as $P(q)$ together with the respective fit to the form factor of polydisperse wormlike chains by Koyama [46]. From this fit we obtain 500 nm for the contour length L, which corresponds to about 57 diblock-copolymer molecules per nanometer of the aggregate and to a linear mass density of 2.8×10^5 g mol^{-1} nm^{-1}. Additionally, the double-logarithmic plot of the data (see inset in Fig. 4) yields a scattering exponent α of 1.04 ± 0.01. This is very close to $\alpha=1$ expected for the rodlike structures. Hence, the assumption that the scattering is dominated by the rodlike particles is justified, since the extrapolation to zero concentration can be done without any knowledge about the number ratio of rods to spheres. The resulting scattering exponent shows that the

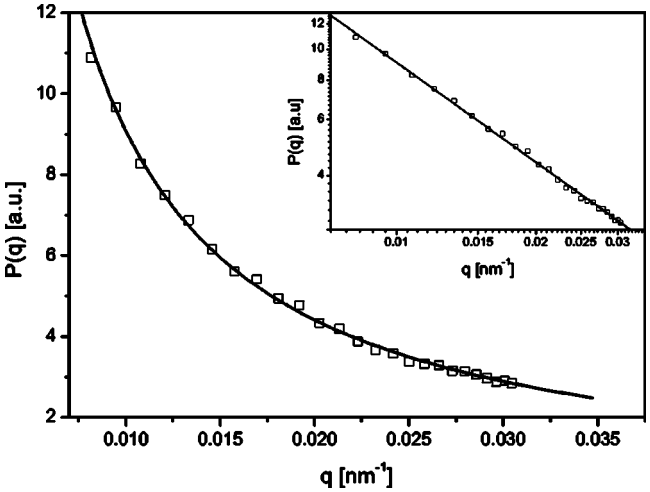

FIG. 4. Static light scattering data for the pure $PB_{40}PEO_{62}$ solution (extrapolated to zero concentration). The solid line represents a fit to a form factor for polydisperse cylinders according to Koyama. The inset shows a log-log plot of the data. The obtained scattering exponent (slope) is -1.04, which is very close to the value expected for rodlike structures.

scattering behavior of the pure polymer solutions is indeed dominated by the rodlike aggregates.

For a rigid rod, the radius of gyration is connected to the aggregate dimensions by

$$R_g^2=\frac{L^2}{12}+\frac{R_{cs}^2}{2}, \tag{24}$$

with R_{cs} the cross-sectional radius of the rod [64]. For elongated thin structures, the second term in this sum is very small compared to the first length-dependent term and can for that reason be omitted here. Using the length computed by applying the Koyama analysis, we compute $R_g=144$ nm as an estimate of the radius of gyration for the rodlike polymer aggregates.

2. Polymer-surfactant mixtures

For the polymer-surfactant mixtures, several different polymer-to-surfactant ratios r_m were prepared, and for each given ratio four to six different concentrations were measured and analyzed using Zimm plots. Figure 3 shows two typical examples for samples with different amount of surfactant (r_m values). Molar mass and radius of gyration were calculated as described above. In Fig. 5, the computed values for R_g are plotted vs concentration. It is obvious that the large aggregates become significantly smaller upon addition of C_{12}TAB, but as already mentioned this result is only a qualitative one. It is also obvious that the curves in Fig. 3 are not linear and therefore the linearization leads to large errors in the computed R_g values. For this reason the values of the radii of gyration, as derived from SANS data will be used further on, especially when discussing the ratio R_g/R_h, which yields information about the shape of the polymer aggregates and the mixed micelles [65].

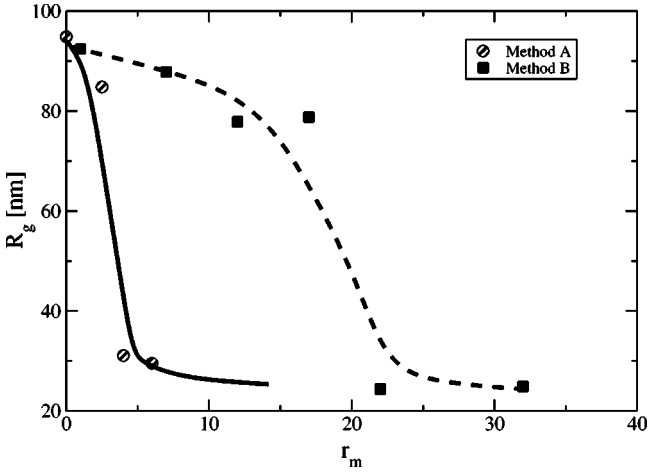

FIG. 5. R_g values as obtained from Zimm plots vs the surfactant-to-polymer ratio r_m. Preparation methods *A* and *B* lead to a different decay behavior, but the final radius of gyration is the same in both cases.

C. Small-angle neutron scattering

Small-angle neutron scattering measurements were carried out for solutions with a polymer mass fraction of 2% and surfactant concentrations covering a range of relative mole fractions r_m from 0 (pure polymer) to 32. In the low-q range ($q<0.02$ Å^{-1}), one observes a decrease of the scattering intensity with increasing r_m (see Fig. 6). In this q range, the scattering curves follow a $1/q^{\alpha}$ dependence with a transition from $\alpha\approx 0.4$ at $r_m=0$ to $\alpha=0$ at $r_m\geqslant 3.3$. Qualitatively, this trend corresponds to a transition from elongated to spherical structures [37].

As the concentration of surfactant increases from 3.3 to 32, the region of zero slope becomes slightly more extended. At higher-q values ($q\geqslant 0.02$ Å^{-1}), the scattering curves $I(q)$ fall off more steeply and the dependence on surfactant concentration is reversed, i.e, $I(q)$ now increases with r_m. All curves exhibit a local minimum at $q>0.05$ Å^{-1} and this minimum is shifted to smaller q values as r_m increases (see

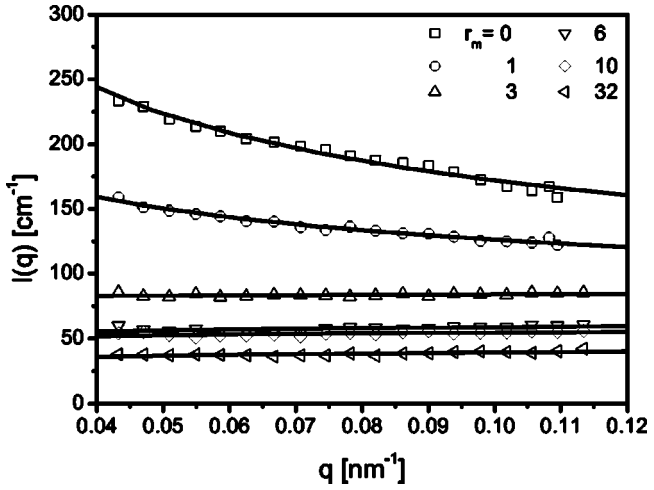

FIG. 6. Low-q parts of the SANS curves. The dashed lines are fits according to $I(q)\propto 1/q^{\alpha}$.

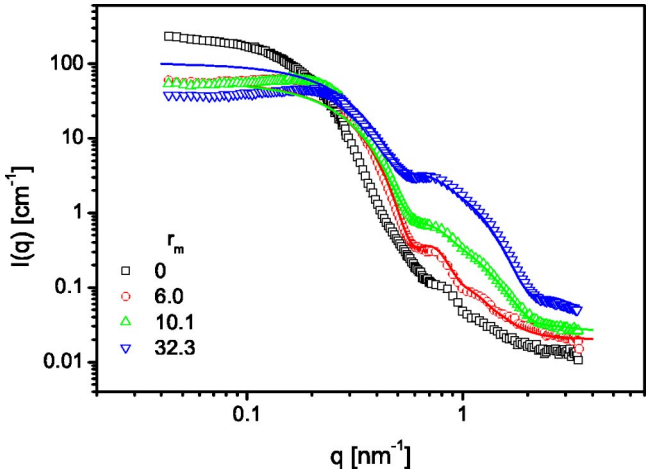

FIG. 7. SANS curves for polymer-surfactant mixtures of different polymer-to-surfactant ratios r_m and fits of the data by sums of two polydisperse sphere form factors (solid lines). Only the spectra from the samples with highest C_{12}TAB concentration have to be described by sums of two distinct particle types, indicating the formation of larger quantities of small micelles, probably consisting of C_{12}TAB.

Fig. 7). These observations conform to the picture of a transformation from the rodlike aggregates into spherical mixed micelles with increasing molar ratio of surfactant to block copolymer.

The measured scattering curves were also analyzed using the indirect Fourier transform (IFT) program by Glatter [40–43]. In the double-logarithmic plot in Fig. 8, the scattering curves can be seen together with the obtained representation of the experimental data. The inset shows the corresponding pair distance distribution functions $p(r)$. For the pure diblock-copolymer solutions, the $p(r)$ curve is a measure of the maximum cross-sectional diameter of the aggregates, without giving any information about the length of the rodlike aggregates. The $p(r)$ curves for the polymer-surfactant system are more complex and reflect the gradual transition to spherical micelles. Although the qualitative features of the $I(q)$ curves do not change as the content of surfactant is gradually increased, the maximum dimension is first slightly decreasing and then remains constant within the experimental precision at $r_m>3.3$. At a relative surfactant mole fraction $r_m=32$, a shoulder in $p(r)$ at low-r values indicates the presence of much smaller particles. Having in mind that the samples for the SANS measurements were prepared by method *A*, i.e., the CMC of C_{12}TAB is exceeded in the SANS samples, these smaller particles can be identified as micelles of pure surfactant coexisting with the polymer-surfactant mixed micelles. The observation of C_{12}TAB micelles indicates that the mixed micelles are saturated with surfactant at this polymer-to-surfactant ratio and thus the added surfactant does not contribute anymore to the overall aggregate dimensions. These findings are in agreement with results recently reported by Bronstein *et al.* [23], which indicate an upper limit for comicellization of polystyrene-*b*-poly(ethyleneoxide) with the surfactant cetylpyridinium chloride. Above a limiting concentration, these authors also

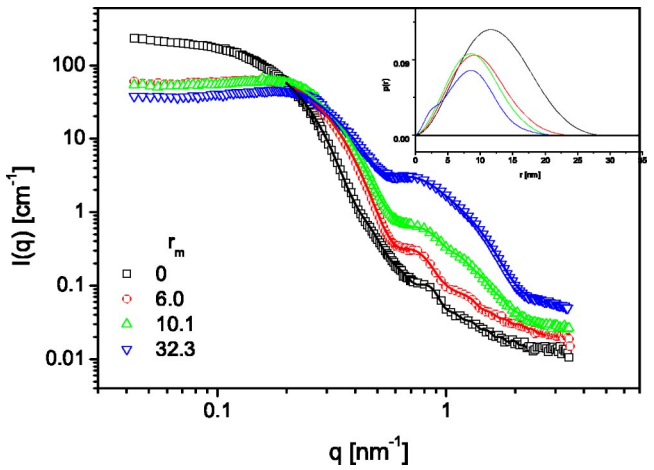

FIG. 8. Analysis of the SANS data of Fig. 7 by the IFT method. The inset shows the computed $p(r)$ functions. The upper curve was obtained for the pure polymer solution, the lower ones for the increasing C_{12}TAB concentrations. Their decay indicates the maximum dimension of the scattering aggregates.

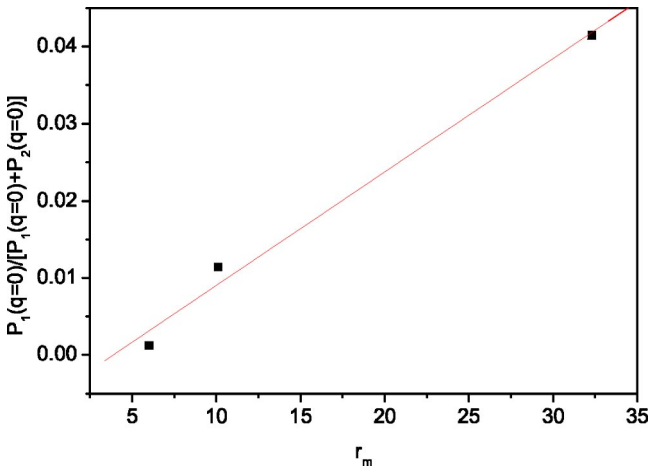

FIG. 9. Ratio of the form factor values extrapolated to $q=0$. For the small (P_1; C_{12}TAB micelles) and the bigger spheres (P_2; mixed polymer-surfactant micelles).

observe the formation of micelles only made of the low-molecular-weight surfactant.

However, for the triblock-copolymer Pluronic mixed with SDS, a different behavior compared to the present study was detected. This anionic surfactant leads to a complete decomposition of the polymer aggregates, ending up with mixed micelles containing only one polymer molecule [24,66]. Similar results were also obtained by Hoffmann and coworkers [26,25].

The SANS data for the polymer-surfactant mixtures were also analyzed in terms of model functions for the form factor $P(q)$ (see Fig. 7). For $P(q)$, we used the integrated form of Eq. (5) and hence a Gaussian size distribution to account for the particle polydispersity. Using a sum of two polydisperse sphere form factors, it was only possible to describe the scattering curves from the three samples with the highest molar ratio of surfactant, $r_m=6$, 10, and 32, but however at low-q values the model curves do not correspond to the experimental curves. This finding is reminiscent of dilute microemulsions, where again only the intermediate and high-q region can be described by form factors [36,67], and can be attributed to a contribution from the structure factor $S(q)$, which was assumed to be one in the used model. A plot of the intensity ratio $I_{small}(q=0)/I_{small}(q=0)+I_{big}(q=0)$ vs concentration, where I_{small} and I_{big} are the contributions of small and large spheres to the overall scattering intensity, leads to a straight line (see Fig. 9). This indicates that the number of small spheres is linearly increasing with growing concentration of surfactant. This again points to the fact that the mixed micelles are already saturated with C_{12}TAB at a molar ratio below 32, as was indicated by the $p(r)$ function resulting from the IFT analysis, and that pure surfactant micelles are present in the solution already at a surfactant-to-polymer ratio $r_m=6$. The radii calculated for the smaller spheres are in good agreement with the size expected for C_{12}TAB micelles (estimated on the basis of the length of the molecule in all-trans configuration). A summary of the radii of gyration R_g extracted from the neutron scattering results is given in Table II.

D. Photon correlation spectroscopy

1. Pure polymer solutions

Solutions of B_{40}-b-EO_{62} were also investigated by photon correlation spectroscopy (also sometimes called DLS). Intensity correlation functions were recorded at five different scattering angles between 30° and 150°. For each scattering angle, the measurements were repeated three times and the values for relaxation rates given below are averages of these three measurements. Figure 10 shows typical examples for the relaxation rate distributions $G(\Gamma)$ analyzing the data using a 100 grid point version of CONTIN (data given were obtained for $c=0.08$ wt%, measured at two different scattering angles). For all samples, two significant contributions were resolved. In some cases, a third contribution at lower frequencies appears which can be attributed to dust particles. The relaxation process with the largest amplitude can be attributed to large rodlike or wormlike micelles consisting of a large number of B_{40}-b-EO_{62} molecules. The assumption of a rodlike or wormlike structure is based on the micrograph in Fig. 1 and the observed high macroscopic viscosity of the samples. Figure 11 shows a plot of the mean relaxation rates of the first mode (largest amplitude) as a function of q^2. A linear dependence is found in all cases. From the slope of this graph, the diffusion coefficients are derived [see Eq. (10)] and these results are shown in Fig. 12. For a pure diffusional mode one expects that Γ is strictly proportional to q^2, i.e., the lines in Fig. 11 should start from the origin. We observe a slight deviation from this behavior which is, however, close to the limit of the experimental error. This deviation may be attributed to the large extension of the rodlike aggregates, which might lead to contributions from rotation or internal bending movements at higher-q values. These motions cannot be separated from the diffusional mode.

Figure 12 shows that in the concentration range studied in this work, only a weak influence of the concentration on the

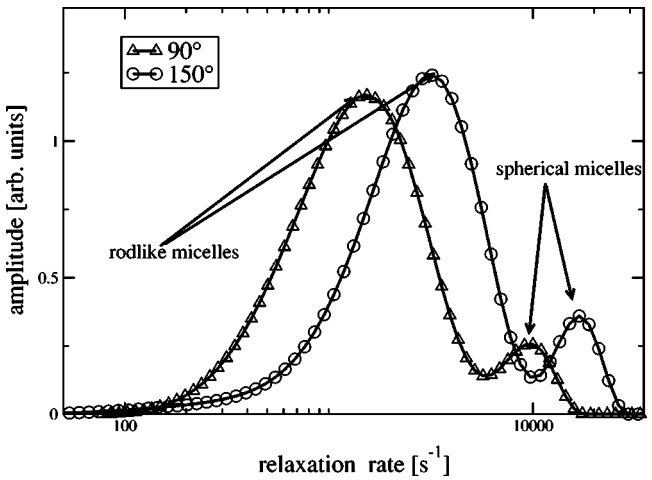

FIG. 10. Typical relaxation rate distributions as obtained by a CONTIN analysis of the experimental correlation functions for the pure polymer solutions (100 transformation grid points). Shown are data for 90° (circles) and 150° (triangles). For 90° scattering angle, two modes are resolved. These we attribute to large rodlike micelles. The second faster relaxation process can be attributed to the smaller spherical micelles also observed in the respective cryo-TEM preparations. At the larger scattering angle of 150°, a third low frequency relaxation appears. This can be attributed to spurious amounts of dust particles.

hydrodynamic size of the aggregates is found. A small concentration dependence like this can be analyzed applying Eq. (13). An extrapolation to zero concentration leads to a self-diffusion coefficient D_0^T of 4.22×10^{-12} m^2/s^{-1}. From this value, we compute a hydrodynamic radius of 58 nm for the rodlike aggregates of B_{40}-*b*-EO_{62}. The observed behavior is in agreement with results obtained for other BCPs (e.g., B_{45}-*b*-EO_{56} [62]).

In Fig. 13, the relaxation frequencies of the faster process

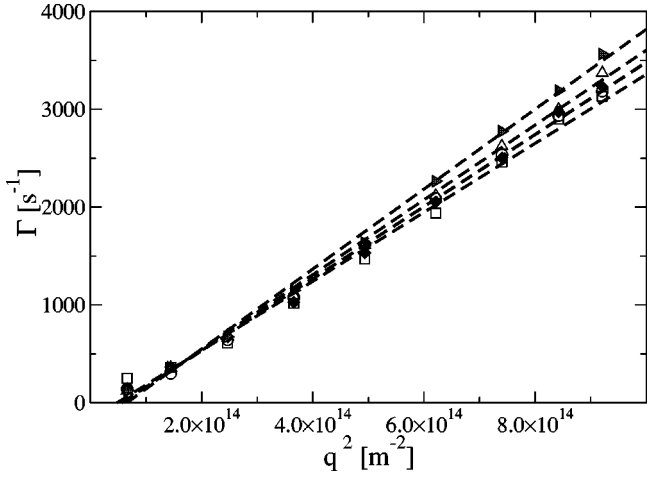

FIG. 11. Plot of the *z*-averaged relaxation rate Γ for the major (slow) relaxational mode vs q^2. For all the investigated concentrations, the observed relaxation mode depends linearly on q^2. At low q a slight deviation is observable, which can be attributed to high length of the aggregates. The investigated concentration range was 0.02–0.2 wt % of polymer.

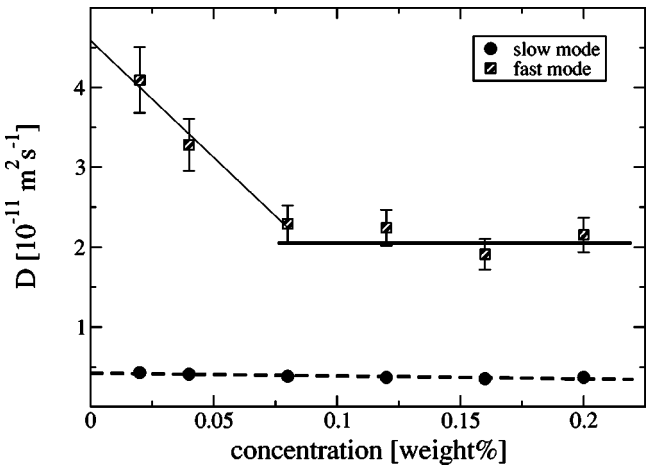

FIG. 12. Diffusion coefficients computed from the slopes in Figs. 11 and 13. For the slow mode (rodlike particles), the experimental error is represented by the size of the symbols. In the investigated interval, the diffusion coefficient associated with the large rodlike aggregates depends only slightly on the B_{40}-*b*-EO_{62} concentration. The dashed line indicates the extrapolation according to Eq. (13). This procedure results in a value of 4.22×10^{-12} m^2 s^{-1}. According to the Stokes-Einstein equation, this leads to a hydrodynamic radius of $\approx$58 nm for the micellar aggregates. The diffusion coefficients for the smaller particles (boxes) exhibit a strong concentration dependence at low polymer weight fraction. The thin solid line indicates a fit according to Eq. (13). The concentration range is 0.02–0.2 wt % of polymer.

are plotted vs q^2. This process too seems to be of diffusional nature in the investigated concentration range and we assign this mode to the smaller—presumably spherical—aggregates observed on the micrographs (see Fig. 1). In the literature, for some block copolymers, monomolecular micelles were observed in selective solvents at low concentrations [68]. For the polymer studied here, such monomolecular micelles would be much smaller than those experimentally observed, and thus we conclude that these spherical micelles also consist of a larger number of polymer molecules.

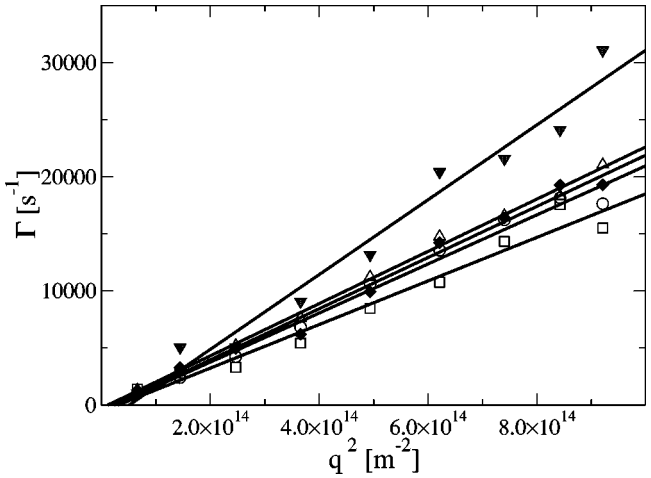

FIG. 13. Plot of the *z*-averaged relaxation rate Γ of the second (fast) mode vs q^2 at several polymer concentrations. (The concentration range is the same as in Fig. 11.)

TABLE I. Results from model calculation for different shapes of the aggregates. For the calculations, a thickness of 14.75 nm for the aggregates was used and the length was chosen to be 435 nm.

Model	D^T (10^{-12} m^2 s^{-1})	D^R (s^{-1})
Garcia de la Torre	4.19	147
Broersma (Newman)	3.85	141
Broersma	3.85	141
Perrin	4.46	185

The concentration dependence of this second relaxation mode is different from that of the large aggregates (see Fig. 12). Although at high concentrations no significant concentration dependence of the translational diffusion coefficient is found, a pronounced linear concentration dependence is seen at low concentrations. An extrapolation according to Eq. (13) using the three data points at the lowest concentrations leads to a D_0^T of 4.59×10^{-13} m^2/s^{-1}. A nonlinear extrapolation of the data of the entire concentration range, using a quadratic expression results in approximately the same value for D_0^T. Based on this translational diffusion coefficient, a hydrodynamic radius of 5.3 nm is calculated for the smaller particles at zero concentration. As already mentioned, the observation of two species is in qualitative agreement with observation of two types of species on electron micrographs (see Fig. 1). However, since the fast mode exhibits a pronounced concentration dependence, the size of the spherical particles observed on the cryo-TEM images (diameter 38.2 nm) should not be compared to the hydrodynamic diameter at infinite dilution but to the value at the highest polymer concentration investigated by DLS. At the highest experimental concentration the fast mode is associated with a hydrodynamic diameter of $\approx$27 nm, which is still smaller than the value observed by cryo-TEM. This discrepancy may be attributed in part to the different concentrations studied in the DLS and the cryo-TEM experiments, which is due to the sample preparation for the cryo-TEM experiments. In addition, the mode contributing with lower amplitude to the decay of the intensity correlation functions may be slightly shifted to higher frequencies, because of the vicinity of the slow mode (attributed to the rodlike structures).

Simple model calculations based on different structural models for rodlike or prolate ellipsoidal shapes lead to the results given in Table I. These calculations are based on a cross-sectional radius of the aggregates of 14.75 nm (estimated on the basis of the SANS data for the pure polymer solutions; see Sec. IV C). The value of the contour length L was adjusted to 435 nm to obtain D^T values matching the experimental result of 4.22×10^{-12} m^2 s^{-1}. This is in rather good agreement with the result from static light scattering, taking into account the crudeness of the approach of neglecting the elasticity of the rodlike structures. From the computed values for D^R (see Table I), it is obvious why the rotational motion cannot be resolved in a VV geometry [69].

Using the radius of gyration R_g calculated in Sec. IV B 1 and the hydrodynamic radius R_h of 58 nm, the ratio R_g/R_h is 2.5. This is a typical value for the rodlike structures [65].

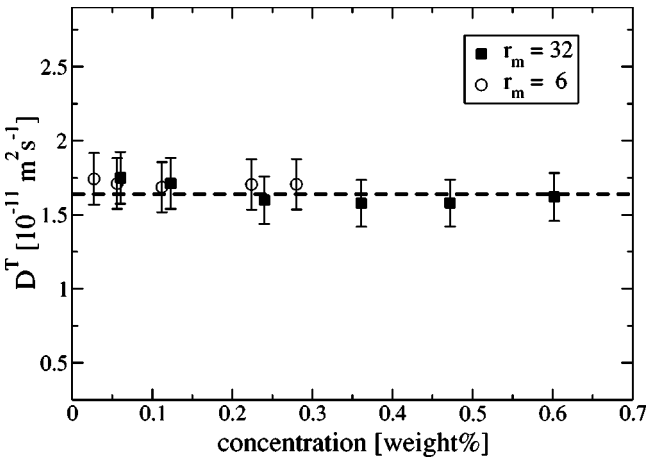

FIG. 14. Plot of the translational diffusion coefficient of the mixed polymer-surfactant micelles vs overall concentration of polymer and surfactant at two polymer-to-surfactant ratios of $r_m=6$ and $r_m=32$. Within the experimental precision (error bars indicate a relative error of 10%), no significant concentration dependence is observed in the entire experimental range. Hence, the end state of the structural transition is already reached at $r_m=6$.

2. Polymer-surfactant mixtures

The mixed samples of polymer and surfactant were also investigated at different scattering angles and concentrations, and the recorded correlation functions were again analyzed using CONTIN. In all cases, only one significant relaxation mode was identified for the mixed systems. In Fig. 14, the D^T values for samples with $r_m=6$ and $r_m=32$ are shown as a function of the overall mass concentration of the dispersed phase. Within the experimental precision, no significant concentration dependence of the translational diffusion coefficient is observable. Moreover, no significant difference between $r_m=6$ and $r_m=32$ can be detected. Therefore, it seems straightforward to use the mean value of the diffusion coefficient, $D^T=1.63\times10^{-11}$ m^2 s^{-1} (indicated by the dashed line in Fig. 14) for the calculation of the hydrodynamic radius. This yields a value $R_h=15$ nm, which appears to be the smallest hydrodynamic radius attainable upon addition of the surfactant C_{12}TAB. This value R_h is reached in samples prepared by both sample preparation methods, *A* and *B*.

Figure 15 shows the hydrodynamic radii computed from DLS results as a function of C_{12}TAB concentration. A drastic decrease of R_h with increasing low-molecular-weight surfactant concentration is observable. This decrease is even more remarkable when taking into account that the total volume fraction of the dispersed phase is increased upon addition of the surfactant. The decrease in hydrodynamic dimension can be explained by a structural transition from elongated structures to spheres. Figure 15 also reveals a significant dependence on the hydrodynamic radius at moderate surfactant concentrations and the method of sample preparation. When the mixed aggregates are prepared such that the CMC of the surfactant is exceeded during the sample preparation, one observes a rather sharp decrease of R_h at relatively low surfactant concentrations. Conversely, when the samples are

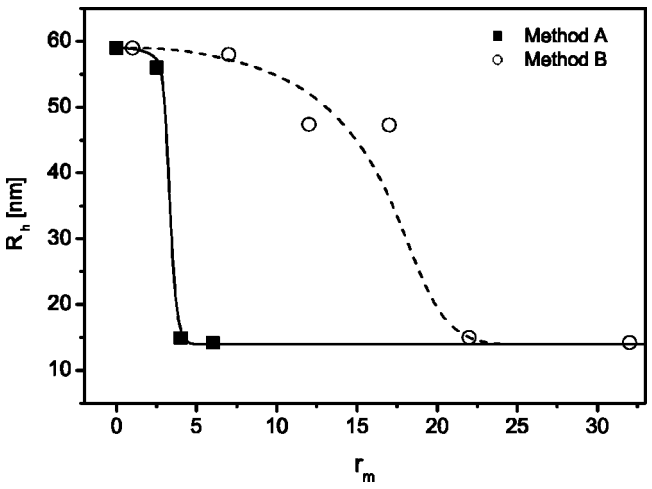

FIG. 15. Hydrodynamic radii (related to the slow mode) as obtained from DLS experiments with increasing C_{12}TAB concentration. Shown are the values for both different preparation methods.

prepared in such a way that the CMC of C_{12}TAB is never exceeded, the decay in hydrodynamic dimensions is broadened and shifted towards higher surfactant concentrations. A possible explanation for this behavior would be kinetic hindrance of the structural rearrangement.

From the radius of gyration as computed on the basis of the SANS experiments on a sample with $r_m = 32$, and the respective hydrodynamic radius of the mixed micelles, the ratio R_g/R_h has the value 0.73. This is very close to the theoretical value for hard spheres [65].

E. Geometrical considerations

The preceding results can be understood by looking at the geometrical parameters of the block-copolymer molecules and the surfactant.

The aggregation number of the rodlike polymer aggregates in the absence of surfactant can be estimated from its radius and the dimensions of a single polymer molecule. The effective volume of a B_{40}-*b*-EO_{62} molecule in water, v_P, estimated on the basis of Tanford's relation [70] is 13.2 nm^3 (4.35 nm^3 for B_{40} plus 8.84 nm^3 for EO_{62}, including two water molecules per oxygen atom). From this value and the volume per unit length of the rodlike aggregates, $V_r = 680$ nm^2 (based on the radius $R_g = 14.75$ nm as obtained by SANS), the aggregate is estimated to contain $N_r = V_r/v_P = 52$ polymer molecules per nanometer, in reasonable agreement with the value of 57 molecules per nanometer obtained from the SLS measurements. This estimated aggregation number corresponds to a mean area per EO_{62} block of ca. 1.8 nm^2 at the outer surface of the aggregates.

The aggregation number of the spherical polymer-surfactant mixed aggregates can be estimated from their volume $V = Nv_P + nv_S$ and surface area $A = Na_P + na_S$, where N and n denote the numbers of polymer and surfactant molecules, v_P and v_S the volumes of polymer and surfactant molecules, a_P and a_S the respective mean "head group" areas. From the radius of the aggregates, $R_g = 7.5$ nm, the Tanford values of the molecular volumes ($v_P = 13.2$ nm^3, $v_S = 0.5$ nm^3), and estimated values of the head group area of the polymer and surfactant in a spherical micelle, $a_P = 2.5$ nm^2 and $a_P = 0.8$ nm^2, we derive an approximate value $N \approx 110$ for the number of polymer molecules in the mixed aggregates. This estimate of the aggregation number is sensitive to the value of R_g (see Table II), but rather insensitive to the chosen values of a_P, a_S, and v_S. The estimated value of N again shows that the mixed aggregates do not represent single-polymer molecules decorated by surfactant, as observed for other types of polymers [23,25,26], but contain a large number of polymer molecules.

TABLE II. Analysis of the SANS data in terms of the indirect Fourier transform (IFT) formalism and the fit by two polydisperse spheres.

		Fit with polydisperse sphere model	
r_m	IFT [40,41,43] R_g^{max} (nm)	R_g mixed micelles (nm)	R_g C_{12}TAB micelles (nm)
0	14.75		
3.3	12.75		
6	12	7.3	1.6
10	11.5	7.0	1.8
32	11	7.5	2.0

V. CONCLUSIONS

The present study has shown that the addition of the cationic surfactant C_{12}TAB to extended rodlike aggregates of the block copolymer B_{40}-*b*-EO_{62} induces a transition to rather monodisperse spherical mixed micelles of polymer and surfactant. These mixed micelles still contain several (of the order of 100) polymer molecules. This behavior is different from findings in other block-copolymer–surfactant systems in which a transition to micelles composed of a single polymer with a larger number of surfactant molecules has been observed.

Pure B_{40}-*b*-EO_{62} forms mainly rodlike aggregates in aqueous solutions. This result is in agreement with findings in previous studies of similar polymers [29,62]. However, for the present polymer these elongated structures coexist with smaller spherical micelles, which were not observed in these earlier studies. The spherical aggregates are clearly recognized in cryo-TEM, but due to their smaller size do not significantly influence the scattering behavior.

The contour length L of the rodlike aggregates is ca. 500 nm (from SLS) and their cross-sectional diameter was determined to be 29.5 nm by means of SANS, agreement with the value of 33.4 ± 3.4 nm obtained by cryo-TEM. An estimate of the contour length L on the basis of the translational diffusion coefficient, applying hydrodynamic models for stiff rods, leads to a value $L = 435$ nm. We attribute the difference between these results to the omission of flexibility in the used hydrodynamic models. The ratio R_g/R_h for the pure polymer aggregates is 2.1 or 2.5, depending on which value for L is used to calculate the radius of gyration. The most important finding of this study is the observation of a structural transition from the rodlike aggregates of the pure poly-

mer to smaller spherical aggregates which is induced by the cationic surfactant. This transition is clearly documented by cryo-TEM and all scattering techniques used in this work. The hydrodynamic radius of the resulting mixed aggregates is ca. 15 nm and the ratio R_g/R_h is 0.73, in agreement with the theoretical value for spheres [65]. The rod-to-sphere structural transition of the present block-copolymer plus surfactant system has a remarkable analogy with a similar transition recently found in aqueous systems of the nonionic surfactant $C_{12}E_5$ by the addition of a fatty alcohol (dodecanol) as a cosurfactant [21]. In the present system, the threshold concentration of the cosurfactant C_{12}TAB at which this transition occurs is dependent on the sample preparation. Tentatively, we attribute this phenomenon to a slow transition kinetics when the C_{12}TAB concentration is always kept below the CMC (sample preparation method *B*). This phenomenon is not yet fully understood and is being further investigated. In agreement with Bronstein *et al.*, we also observe that there exists a threshold concentration for the low-molecular-weight surfactant. Above this concentration additional surfactant is not incorporated in mixed micelles, but forms small micelles on its own. However, preliminary studies with a different surfactant (SDS) indicate that this behavior is not universal [24]. Currently, investigations are in progress studying the effect of SDS on the B_{40}-*b*-EO_{62} aggregates [71].

ACKNOWLEDGMENTS

This work was supported by the Deutsche Forschungsgemeinschaft through the Sonderforschungsbereich 448. The neutron scattering experiments were financed by the European Union (HIPRI). The authors would also like to thank the Laboratoire Léon Brillouin (laboratoire commun CEA-CNRS) for providing beam time and are grateful to Alain Lapp for help with the PAXY machine.

[1] V.N. Manoharan, A. Imhof, J.D. Thorne, and D.J. Pine, Adv. Mater. (Weinheim, Ger.) **13**, 447 (2001).
[2] A.E. Larson and D.G. Grier, Nature (London) **385**, 230 (1997).
[3] R. Strey, Curr. Opin. Colloid Interface Sci. **1**, 402 (1996).
[4] D. Langevin, Annu. Rev. Phys. Chem. **43**, 341 (1992).
[5] T. Hellweg, Curr. Opin. Colloid Interface Sci. **7**, 50 (2002).
[6] S. Förster, Ber. Bunsenges. Phys. Chem. **101**, 1671 (1997).
[7] A.C. Edrington, A.M. Urbas, P. DeRege, C.X. Chen, T.M. Swager, N. Hadjichristidis, M. Xenidou, L.J. Fetters, J.D. Joannopoulos, Y. Fink, and E.L. Thomas, Adv. Mater. (Weinheim, Ger.) **13**, 421 (2001).
[8] H.-P. Hentze, E. Krämer, B. Berton, S. Förster, M. Antonietti, and M. Dreja, Macromolecules **32**, 5803 (1999).
[9] I.W. Hamley, S.-M. Mai, A.J. Ryan, J.P.A. Fairclough, and C. Booth, Phys. Chem. Chem. Phys. **3**, 2972 (2001).
[10] B. Chu, Langmuir **11**, 414 (1995).
[11] H. Otsuka, Y. Nagasaki, and K. Kataoka, Curr. Opin. Colloid Interface Sci. **6**, 3 (2001).
[12] V.N. Bogomolov, S.V. Gaponenko, I.N. Germanenko, A.M. Kapitonov, E.P. Petrov, N.V. Gaponenko, A.V. Prokofiev, A.N. Ponyavina, N.I. Silvanovich, and S.M. Samoilovich, Phys. Rev. E **55**, 7619 (1997).
[13] D.C. Wang and A.P. Gast, J. Phys.: Condens. Matter **11**, 10 133 (1999).
[14] H. Miguez, F. Meseguer, C. Lopez, F. Lopez-Tejeira, and J. Sanchez-Dehesa, Adv. Mater. (Weinheim, Ger.) **13**, 393 (2001).
[15] T. Palberg, J. Phys.: Condens. Matter **11**, R323 (1999).
[16] T. Hellweg, C.D. Dewhurst, E. Brückner, K. Kratz, and W. Eimer, Colloid Polym. Sci. **278**, 972 (2000).
[17] J. Bibette, J. Colloid Interface Sci. **147**, 474 (1991).
[18] L. Bronstein, E. Krämer, B. Berton, C. Burger, S. Förster, and M. Antonietti, Chem. Mater. **11**, 1402 (1999).
[19] T. Hellweg and R. von Klitzing, Physica A **283**, 349 (2000).
[20] U. Menge, P. Lang, and G. Findenegg, Colloids Surf., A **163**, 81 (2000).
[21] U. Menge, P. Lang, and G.H. Findenegg, J. Phys. Chem. B **107**, 1316 (2003).
[22] M. Regenbrecht, S. Akari, S. Förster, and H. Möhwald, J. Phys. Chem. B **103**, 6669 (1999).
[23] L.M. Bronstein, D.M. Chernyshov, E. Vorontsov, G.I. Timofeeva, L.V. Dubrovina, P.M. Valetsky, S. Kazakov, and A.R. Khokhlov, J. Phys. Chem. B **105**, 9077 (2001).
[24] Y. Li, R. Xu, D.M. Bloor, J.F. Holzwarth, and E. Wyn-Jones, Langmuir **16**, 10515 (2000).
[25] E. Hecht, K. Mortensen, M. Gradzielski, and H. Hoffmann, J. Phys. Chem. **99**, 4866 (1995).
[26] H. Hoffmann, Tenside Surfactants Detergents **32**, 462 (1995).
[27] B. Jakobs, T. Sottmann, R. Strey, J. Allgaier, L. Willner, and D. Richter, Langmuir **15**, 6707 (1999).
[28] H. Endo, J. Allgaier, G. Gompper, B. Jakobs, M. Monkenbusch, D. Richter, T. Sottmann, and R. Strey, Phys. Rev. Lett. **85**, 102 (2000).
[29] H. Egger, A. Nordskog, and P. Lang, Macromol. Symp. **162**, 291 (2000).
[30] S. Broersma, J. Chem. Phys. **32**, 1626 (1960).
[31] S. Broersma, J. Chem. Phys. **32**, 1632 (1960).
[32] F. Perrin, J. Phys. Radium **5**, 497 (1934).
[33] F. Perrin, J. Phys. Radium **7**, 1 (1936).
[34] S.H. Koenig, Biopolymers **14**, 2421 (1975).
[35] T. Hellweg and D. Langevin, Physica A **264**, 370 (1999).
[36] M. Gradzielski, D. Langevin, and B. Farago, Phys. Rev. E **53**, 3900 (1996).
[37] T. Gutberlet, M. Kiselev, H. Heerklotz, and G. Klose, Physica B **276-278**, 381 (2000).
[38] O. Glatter and O. Kratky, *Small Angle X-ray Scattering* (Academic Press, London, 1982).
[39] D.J. Cebula, R.H. Ottewill, J. Ralston, and P. Pusey, J. Chem. Soc., Faraday Trans. 1 **77**, 2585 (1981).
[40] O. Glatter, Acta Phys. Austriaca **47**, 83 (1977).
[41] O. Glatter, J. Appl. Crystallogr. **10**, 415 (1977).
[42] O. Glatter, J. Appl. Crystallogr. **13**, 7 (1980).
[43] O. Glatter, R. Strey, K.-V. Schubert, and E.W. Kaler, Ber. Bunsenges. Phys. Chem. **100**, 323 (1996).
[44] P. Hiemenz, *Principles of Colloid and Surface Chemistry*

(Marcel Dekker, New York, 1977).
[45] T.M. Bender, R.J. Lewis, and R. Pecora, Macromolecules **19**, 244 (1986).
[46] R. Koyama, J. Phys. Soc. Jpn. **34**, 1029 (1973).
[47] B.J. Berne and R. Pecora, *Dynamic Light Scattering* (Wiley, New York, 1976).
[48] B. Chu, *Laser Light Scattering* (Academic Press, New York, 1974).
[49] K.S. Schmitz, *An Introduction to Dynamic Light Scattering by Macromolecules* (Academic Press, New York, 1990).
[50] D.E. Koppel, J. Chem. Phys. **57**, 4814 (1972).
[51] S.W. Provencher, Comput. Phys. Commun. **27**, 213 (1982).
[52] S.W. Provencher, Comput. Phys. Commun. **27**, 229 (1982).
[53] J. Riseman and J.G. Kirkwood, J. Chem. Phys. **18**, 512 (1950).
[54] P.S. Russo, in *Dynamic Light Scattering*, edited by W. Brown (Clarendon Press, Oxford, 1993), Chap. 12
[55] M. Tirado and J. Garcia de la Torre, J. Chem. Phys. **71**, 2581 (1979).
[56] M.M. Tirado and J. Garcia de la Torre, J. Chem. Phys. **73**, 1986 (1980).
[57] M.M. Tirado, C.L. Martinez, and J.G. de la Torre, J. Chem. Phys. **81**, 2047 (1984).
[58] S. Förster and E. Krämer, Macromolecules **32**, 2783 (1999).
[59] H. Schlaad, H. Kukula, J. Rudloff, and I. Below, Macromolecules **34**, 4302 (2001).
[60] The document is available on the web: http://www-llb.cea.fr/spectros/spectros-llb.pdf
[61] J.P. Cotton, in *Neutron, X-Ray and Light Scattering*, edited by P. Lindner and T. Zemb (Elsevier Science, B.V., Amsterdam, 1991).
[62] Y. Zheng, Y.-Y. Won, F.S. Bates, H.T. Davis, L.E. Scriven, and Y. Talmon, J. Phys. Chem. **103**, 10 331 (1999).
[63] Y. Talmon, Ber. Bunsenges. Phys. Chem. **100**, 364 (1996).
[64] W. Brown, *Dynamic Light Scattering* (Clarendon Press, Oxford, 1993).
[65] W. Burchard, Chimia **39**, 10 (1985).
[66] Y. Li, R. Xu, S. Couderc, D.M. Bloor, E. Wyn-Jones, and J.F. Holzwarth, Langmuir **17**, 183 (2001).
[67] T. Hellweg, A. Brûlet, and T. Sottmann, Phys. Chem. Chem. Phys. **2**, 5168 (2000).
[68] Y. Liu, S.-H. Chen, and J.S. Huang, Macromolecules **31**, 6226 (1998).
[69] R. Pecora, J. Chem. Phys. **49**, 1036 (1968).
[70] C. Tanford, *Physical Chemistry of Macromolecules* (Wiley, New York, 1961).
[71] A. Nordskog, H. Egger, G.H. Findenegg, and T. Hellweg (unpublished).